Check for updates

ADVANCED ELECTRONIC MATERIALS
Open Access
www.advelectronicmat.de

Development of a Triboelectric Nanogenerator for Joining of Silver Nanorods

Mohammad Amin Jalili, Fathallah Karimzadeh, Mohammad Hossein Enayati, Ehsan Naderi Kalali, and Noushin Raeisi Kheirabadi**

On account of their excellent properties, 2D nanostructures beyond graphene, such as MoS_2, have extensive applications. Given their quantum confinement effects, MoS_2 monolayers could efficiently trap electrons as an intermediate layer between friction and electrode in triboelectric nanogenerators (TENGs) and successfully hinder their recombination and air breakdown, increasing their output. With the help of this phenomenon, a TENG called PS+PS/MoS_2-AHSG (PPMA) TENG is fabricated with an open-circuit voltage of ≈1200 V and a short-circuit current of 0.74 mA, and a maximum power of 11.27 mW. PPMA TENG consists of transparent polystyrene (PS) and PS/MoS_2 as negative contact and storage layers. Also, the positive layer is a novel Alyssum homolocarpum seed gum (AHSG) layer, which is a natural polymer. This TENG could successfully light up 115 commercial light-emitting diodes. PPMA TENG exhibits exceptional mechanical robustness so that after a decrease in its outputs, heating would activate the self-healing mechanism, and the surface charge density could reach from 0.428 to 0.874 μC m^{-2}, which is 82% of the initial value. To demonstrate the practical applications of PPMA TENG as a high-voltage sustainable power source, it is successfully employed to perform a dielectrophoretic assisted welding of silver nanorods.

1. Introduction

Since the invention of triboelectric nanogenerators (TENGs),[1] many studies have been conducted to improve the output performance of these devices.[2,3] After electron generation on the friction layer of TENG, according to contact electrification, surface charge density would drop gradually.[4] Air breakdown is the main reason for charge loss in TENGs.[5] Air breakdown happens when the applied electrical field between the friction couple of a TENG exceeds a certain value making the air between them become partially conductive. Therefore, a discharge happens, reducing the tribo-charges on the surface of contact layers.[6,7] Another critical mechanism of charge loss is charge recombination due to the combination of surface charges with oppositely charged particles in the air or opposite induced charges.[7] Charge loss could occur with other effects such as drift[4] and diffusion.[8]

Introducing an intermediate charge storage layer with a charge trap ability could successfully hinder air breakdown and prevent charge dissipation. This intermediate layer, located between the electrode and friction layer, simply traps the charges and suppresses the migration of charges to the electrode.[9,10] This layer could be made of an organic polymer or a polymeric composite with charge trapping ability, For instance, polystyrene (PS) as an organic polymer could trap charges due to discontinuity of energy caused by the benzene ring structure.[11] Moreover, additive physical modification is a strategy to create polymeric composites with charge-trapping ability.[12] Embedding additives with large surface area and electron trapping ability in the intermediate layer could improve the output of TENGs;[2] for instance, Wu et al.[13] developed a TENG with a stacked structure in which embedded reduced graphene oxide (rGO) nanoflakes as electron traps into the polyimide (PI). Their findings revealed that rGO nanoflakes could act as

M. A. Jalili, F. Karimzadeh, M. H. Enayati
Department of Materials Engineering
Isfahan University of Technology
Isfahan 84156-83111, Iran
E-mail: karimzadeh_f@iut.ac.ir

The ORCID identification number(s) for the author(s) of this article can be found under https://doi.org/10.1002/aelm.202201348.

© 2023 The Authors. Advanced Electronic Materials published by Wiley-VCH GmbH. This is an open access article under the terms of the Creative Commons Attribution License, which permits use, distribution and reproduction in any medium, provided the original work is properly cited.

DOI: 10.1002/aelm.202201348

E. N. Kalali
Faculty of Geosciences and Environmental Engineering
Southwest Jiaotong University
Chengdu 610031, P. R. China

E. N. Kalali
Department of polymer processing
Institute of Macromolecular Chemistry
Czech Academy of Sciences
Heyrovského náměstí 2, Prague 6 16200, Czech Republic

N. R. Kheirabadi
Unconventional Computing Laboratory
University of the West of England
Bristol BS16 1QY, UK
E-mail: noushin.raeisikheirabadi@uwe.ac.uk

electron traps and prevent charge loss. It was demonstrated that rGO nanoflakes could suppress the recombination of generated negative with positive charges. The aforementioned TENG exhibited a power density of 6.3 W m^{-2} which was 30 times greater than TENG without the PI-rGO layer. Aside from rGO, other materials, such as graphene oxide,[14] titania,[15] and MoS_2,[16] could operate as electron traps. In another research, Wu et al.[16] investigated a TENG with MoS_2/PI electron trap layer with 25.7 W m^{-2}, which is 120 times more than that of the device without MoS_2 monolayer. The open-circuit voltage of TENG with MoS_2 was 400 V.

Among nanomaterials, with electron-accepting characteristics, 2D MoS_2 has exceptional properties.[17] MoS_2 is a transition metal dichalcogenide (TMD) having a Mo layer sandwiched between two sulfur layers, typically in a hexagonal configuration. These monolayers consist of three sub-layers (S-Mo-S) held together with van der Waals forces in bulk MoS_2, which are several orders of magnitude weaker than in-plane covalent bonds.[18,19] Therefore, exfoliation of bulk MoS_2 is a facile approach for producing single- and/or few-layer MoS_2.[20,21] MoS_2 flakes are semiconductors with a tunable bandgap that ranges from 1.2 eV indirect bandgap at Γ point of the Brillouin zone in bulk to 1.8 eV direct bandgap at K point in single layer form.[22,23] This bandgap tunability is caused by quantum confinement effects leading to alterations in hybridization between p_z orbitals of sulfur atoms and d_z^2 orbitals of molybdenum near Γ point, which manifests in a downward energy shift at Γ point with thickness reduction or a rise in interlayer separation distance. Ultimately, thinning down the thickness of MoS_2 flakes to monolayer results in an indirect to direct bandgap transition.[24–26] High surface-to-volume ratio, flexibility, and chemical stability along with semiconducting properties made 2D MoS_2 ideal for the fabrication of various thin and transparent flexible electronic devices, wearable devices, and body implantation devices, as well as TENGs.[27]

Seol et al.[28] investigated triboelectric properties of various layered 2D materials and concluded that MoS_2 exhibited the most tribo-negative properties among $MoSe_2$, graphene, graphene oxide, WS_2, and WSe_2, and it was located in the triboelectric series between polydimethylsiloxane (PDMS) and polytetrafluoroethylene (PTFE). The superior negative triboelectric charging of MoS_2 was linked to its highly effective work function (4.85 eV). The voltage and current of the fabricated TENG with MoS_2 as negative and Nylon as positive contact material reached 7.48 V and 0.82 μA respectively, with a power density of 36.3 mW m^{-2}. Several studies have investigated negative contact materials based on MoS_2 in TENGs.[28–31] Moreover, Wu et al. suggested using MoS_2 as an electron trap material below negative contact material with high efficiency and outstanding outputs.[16]

Currently, TENGs have been suggested to be employed in various fields. TENGs' application could be divided into four main categories including blue energy, micro/nano power sources, self-powered sensors, and high voltage power sources.[32] Considering the output characteristics of TENGs, they could act as high-voltage power sources for a variety of novel and state-of-the-art applications.[33] For example, Cha et al.[34] reported a cold-welding method using a non-uniform electric field created by an alternate current (AC) function generator between two electrodes. In this method, the non-uniform electric field would induce dielectrophoresis (DEP) force[35] between gold nanoparticles leading to cold-welding of gold nanoparticles and fabrication of nanoribbons. According to the AC nature of contact-separation TENGs as an alternative to function generators, TENGs could act as the power source for the cold-welding of nanoparticles.

In this work, a novel PS/MoS_2 nanocomposite was employed for both the negative contact layer and electron-accepting layer with a PS and PS/MoS_2 bilayer structure. The structure and thickness of the negative layer were optimized with a new positive contact layer made of Alyssum homolocarpum seed gum (AHSG), which is a natural polymer introduced to prepare the PS+PS/MoS_2-AHSG (PPMA) TENG and it was subsequently optimized. The prepared TENG was utilized to perform a welding process on silver nanorods (Ag NRs).

2. Results and Discussion

To investigate the surface morphological features of fabricated layers, scanning electron microscopy (SEM) characterization was performed on AHSG, PS, and PS/MoS_2 layers (**Figure 1**a–c). It could be inferred that there are no significant surface features in all of the layers. Therefore, surface roughness does not dramatically affect the variations in the output of TENGs, but, these variations are rooted in suitable materials selection and the electron trapping ability of MoS_2. Figure 1d shows a cross-section view of PS+PS/MoS_2 layers and their corresponding indium tin oxide/polyethylene terephthalate (ITO/PET) substrate. The difference between PS and PS/MoS_2 is obvious due to their dissimilar contrast and also their thickness was 35 and 25 μm, respectively.

Moreover, the UV–vis spectrum of MoS_2 dispersion is presented in Figure 1e. Two A and B peaks at 613 and 675 nm stem from direct-gap transition at the K point of the Brillouin zone, indicating successful exfoliation of MoS_2 and synthesis of monolayers. To further characterize the exfoliated MoS_2 flakes, transmission electron microscopy (TEM) images of the sample were obtained (Figure 1f). This is also another indication of the successful synthesis of monolayer MoS_2, which has a large surface area and superior electron-trapping properties. The presented flake has a 124 × 70 nm size and approximately an area of 7572 nm.

To evaluate the role of MoS_2 monolayer efficiency as a contact material or as a charge trap TENGs with PS, PS/MoS_2, PS+PS/MoS_2, and PS+PS negative layers were fabricated. In order to compare the fabricated TENGs, their voltage was measured under 8 N force with a 4 Hz frequency. As shown in **Figure 2**a, the average voltage of PS TENG was 74.20 V, while the average voltage of PS/MoS_2 TENG was 338.89 V. This evidence demonstrates that the MoS_2 as a contact material has a tendency to charge negatively upon contact. This tendency could be attributed to the surface density of states and the effective work function of contact materials.[13,36,37] Since MoS_2 has a higher work function than the tribo-positive material (in this case, PET), charge transfer will occur from the filled electronic states of the tribo-positive material during contact electrification. Therefore, due to the presence of MoS_2, the effective work function

© 2023 The Authors. Advanced Electronic Materials published by Wiley-VCH GmbH

2199160x, 2023, 5, Downloaded from https://onlinelibrary.wiley.com/doi/10.1002/aelm.202201348 by Test, Wiley Online Library on [22/05/2023]. See the Terms and Conditions (https://onlinelibrary.wiley.com/terms-and-conditions) on Wiley Online Library for rules of use; OA articles are governed by the applicable Creative Commons License

ADVANCED ELECTRONIC MATERIALS
Open Access
www.advelectronicmat.de

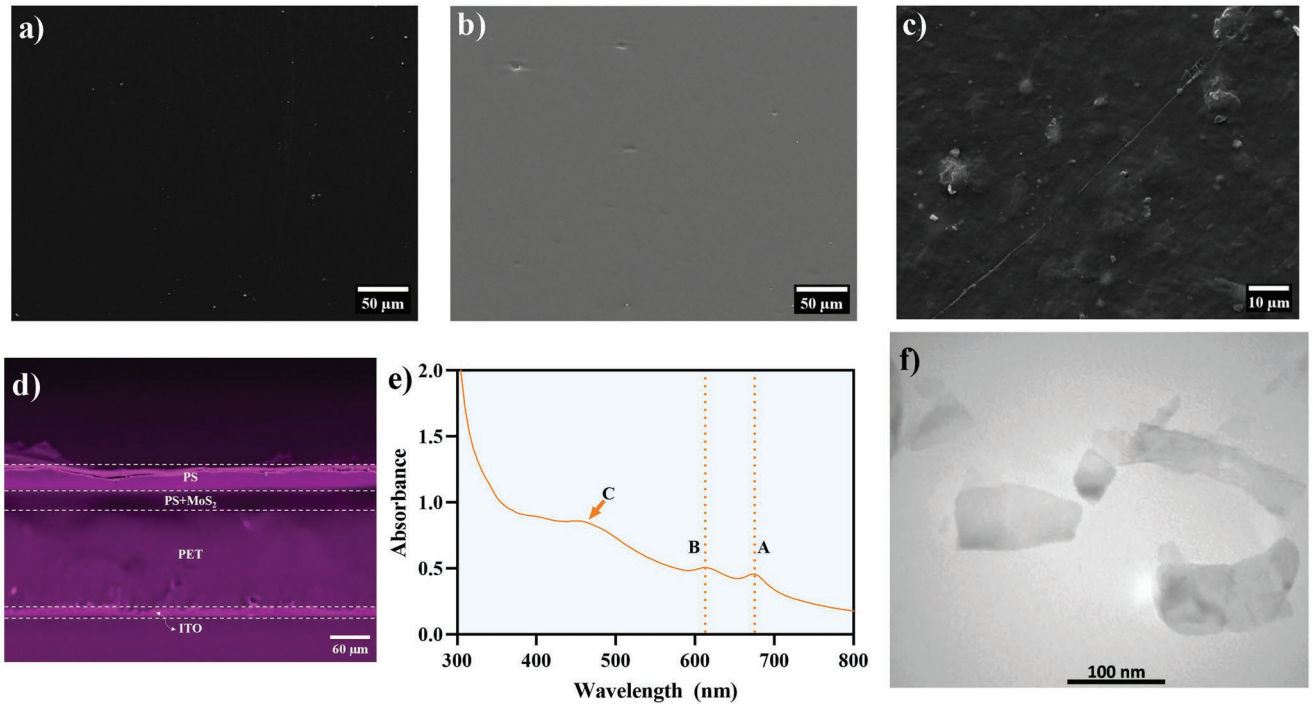

Figure 1. SEM image of layers and MoS_2 monolayers characterization. SEM image of a) PS, b) PS/MoS_2, c) AHSG, d) cross-section of PS+PS/MoS_2 layers, e) UV–vis spectra, and f) TEM images of exfoliated MoS_2 monolayers.

difference between triboelectric contact layers was increased and as a result, the amount of created charge on the surface of the PS/MoS_2 layer was higher than that of the PS layer.[13] More importantly, the average voltages of PS+PS TENG and PS+PS/MoS_2 TENG were 52.84 and 615.99 V, respectively. The voltage saw a 12-fold growth once the MoS_2 nanocomposite was incorporated into the TENG. Wu et al.[16] highlighted the existence of electrons in MoS_2 by fabricating a floating-gate metal-insulator-semiconductor (MIS) device and studying its capacitance–voltage curves. The behavior of MoS_2 nanocomposite-based MIS was similar to that of a typical p-Si-based MIS device with charge-trapping regions. The presence of such sites could be attributed to the electron-trapping effect of the MoS_2 in the polymeric nanocomposite. It was reported that the captured electrons could occupy both energy states at trap sites on the interface of MoS_2 and the bottom of the conduction band.[16] The probability of electron occupation is greater for energies below the Fermi energy level, due to the Fermi–Dirac distribution.[38]

To explore further the influence of MoS_2 concentration on PS+PS/MoS_2 and PS/MoS_2 TENGs, TENGs with various concentrations were fabricated and their voltage was evaluated to optimize the concentration of MoS_2 in nanocomposites. The concentration of MoS_2 dispersion in *N*-methyl-2-pyrrolidone (NMP) was estimated using the Bear–Lambert method (Figure S1, Supporting Information). According to Figure 2e, PS/MoS_2 by raising the amount of exfoliated MoS_2 in PS/MoS_2 nanocomposite from 0.007 ± 0.0003 to 0.0300 ± 0.0003 mg only a moderate escalation of 32% from 500.3 to 662.4 was observed in average voltage which could be assigned to MoS_2 inclination to charge negatively during contact electrification. This was different in PS+PS/MoS_2 TENG. Evidently, the PS+PS/MoS_2 TENG with 0.0300 ± 0.0003 mg (0.002 wt%) MoS_2 exhibited the maximum output (772 V). With respect to the compared values of voltages, PS+PS/MoS_2 TENG with 0.002 wt% MoS_2 had the greatest output owing to the existence of an electron-accepting layer, which inhibits charge loss and causes charges to be stored below the contact layer in PS/MoS_2 nanocomposite.

This section investigates the influence of thickness in PS and PS/MoS_2 layers. Two groups of TENGs were fabricated. One group with variable PS/MoS_2 thickness and a 35 µm PS, whereas the other had variable PS thickness and a 25 µm PS/MoS_2 layer. First of all, the thickness of the PS/MoS_2 layer was optimized. By rising the spin-coating speed and consequently decreasing the thickness of the PS+PS/MoS_2 bottom layer from 94 to 25 µm, the voltage substantially soared from 463.54 to 828.45 V. By decreasing thickness to 15 µm, the open-circuit voltage was reduced to 624.24 V (**Figure 3**). Cui et al.[4] observed the same trend for the electron trap layer, indicating that the majority of the triboelectric charges are stored in the bottom layer. The top layer's thickness varied from 35 to 15 µm and the open-circuit voltage dwindled from 964.15 to 756.32 V (Figure 3). After selecting the best configuration of negative layers, its application as a single-electrode mode TENG was examined.

A 7 × 3 cm^2 ITO/PET substrate was spin-coated with PS/MoS_2 then PS and placed on the touchscreen of a smartphone just above the keyboard. **Figure 4**a shows the output of the setup when typing. The inset picture illustrates the energy harvesting layer on the smartphone screen, indicating the high transparency of the PS+PS/MoS_2 bilayer. To further investigate the transparency of triboelectric layers, UV–vis spectra of

© 2023 The Authors. Advanced Electronic Materials published by Wiley-VCH GmbH

2199160x, 2023, 5, Downloaded from https://onlinelibrary.wiley.com/doi/10.1002/aelm.202201348 by Test, Wiley Online Library on [22/05/2023]. See the Terms and Conditions (https://onlinelibrary.wiley.com/terms-and-conditions) on Wiley Online Library for rules of use; OA articles are governed by the applicable Creative Commons License

ADVANCED ELECTRONIC MATERIALS
Open Access
www.advelectronicmat.de

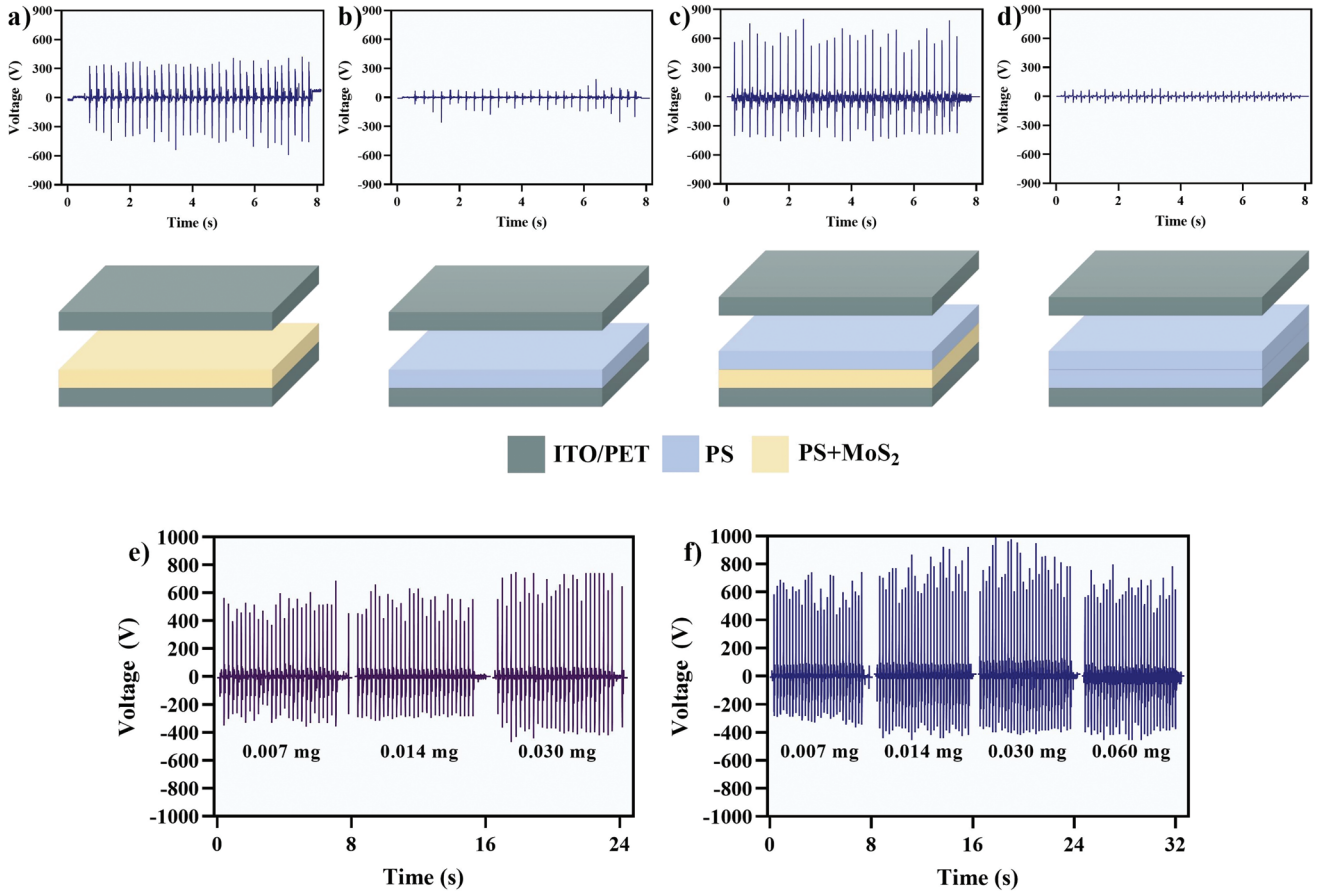

Figure 2. Output comparison of fabricated TENGs. Voltage of a) PS/MoS_2 TENG, b) PS TENG, c) $PS+PS/MoS_2$ TENG, and d) PS+PS TENG. Voltage of e) PS/MoS_2 TENG and f) $PS+PS/MoS_2$ TENG with different MoS_2 concentrations.

PS, PS/MoS_2, and $PS+PS/MoS_2$ were measured in the visible light range (400–800 nm wavelength) and the transparency of PS, PS/MoS_2, and $PS+PS/MoS_2$ was 97.44%, 96.82%, and 96.73%, respectively (Figure 4b). All of the fabricated layers had high transparency even the bilayer structure. Following complete negative layer optimization, the concentration of positive AHSG layer was performed and the result is available in Figure S2, Supporting Information, then a TENG composed of

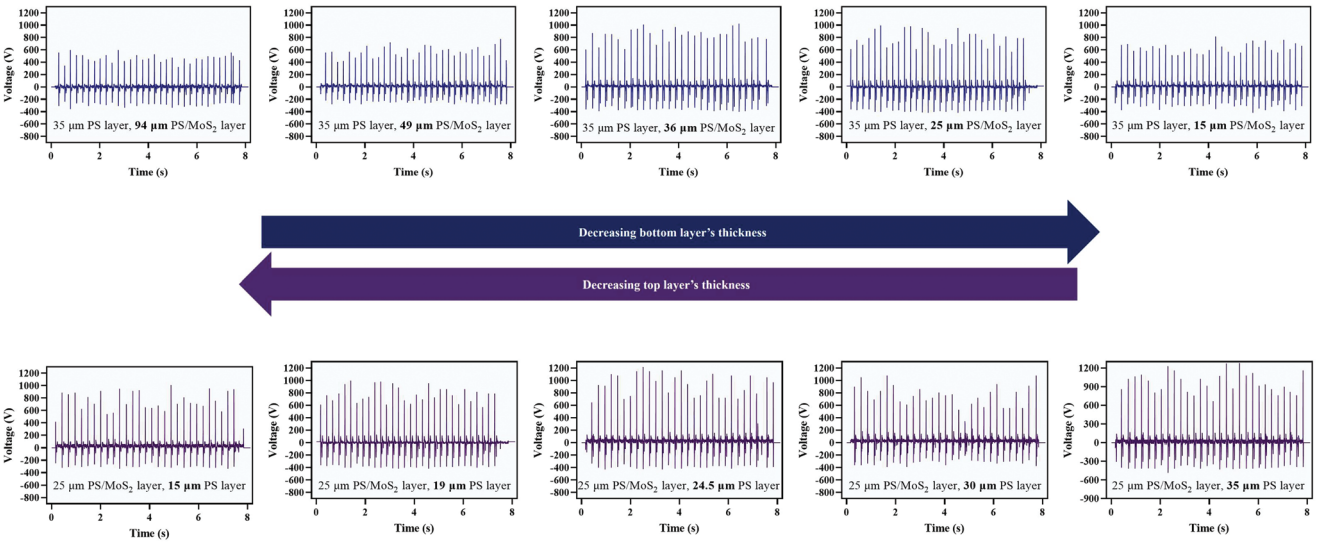

Figure 3. Thickness effects. Voltage of $PS+PS/MoS_2$ TENG with decreasing PS/MoS_2 layer.

© 2023 The Authors. Advanced Electronic Materials published by Wiley-VCH GmbH

2199160x, 2023, 5, Downloaded from https://onlinelibrary.wiley.com/doi/10.1002/aelm.202201348 by Test, Wiley Online Library on [22/05/2023]. See the Terms and Conditions (https://onlinelibrary.wiley.com/terms-and-conditions) on Wiley Online Library for rules of use; OA articles are governed by the applicable Creative Commons License

ADVANCED ELECTRONIC MATERIALS
Open Access
www.advelectronicmat.de

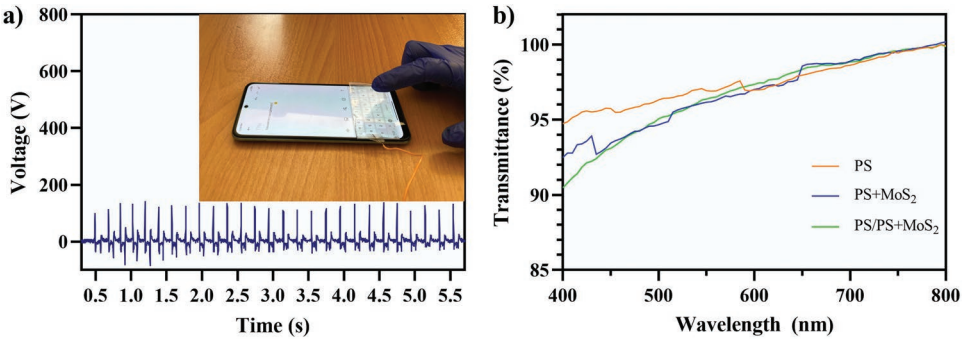

Figure 4. Transparency of fabricated layers. a) Voltage of PS+PS/MoS_2 tapped with one finger on a smartphone touchscreen and b) transmittance of PS, PS/MoS_2, and PS+PS/MoS_2 layers in the visible region.

PS+PS/MoS_2 layer and AHSG as positive layer named PPMA TENG was fabricated and further optimized.

After fabrication, the output of the PPMA TENG was measured under various forces ranging from 2 to 10 N. Under 8 N, the voltage reached its peak value of ≈800 V, which is twice as high as the output under 2 N. By increasing the applied force to 10 N, the output dropped to 400 V (**Figure 5**a). Subsequently, the frequency response of PPMA TENG was investigated under 1–6 Hz. As demonstrated in Figure 5b, PPMA TENG performed better under 4.5 Hz frequency, with the maximum voltage exceeding 900 V, which is three times higher than the voltage under 1 Hz. This improvement in the performance of PPMA TENG could be associated with a rise in the average velocity of the applied force by increasing the frequency. This tendency, however, is only maintained for frequencies up to 4.5 Hz. Output diminished at frequencies higher than 4.5 Hz. This phenomenon

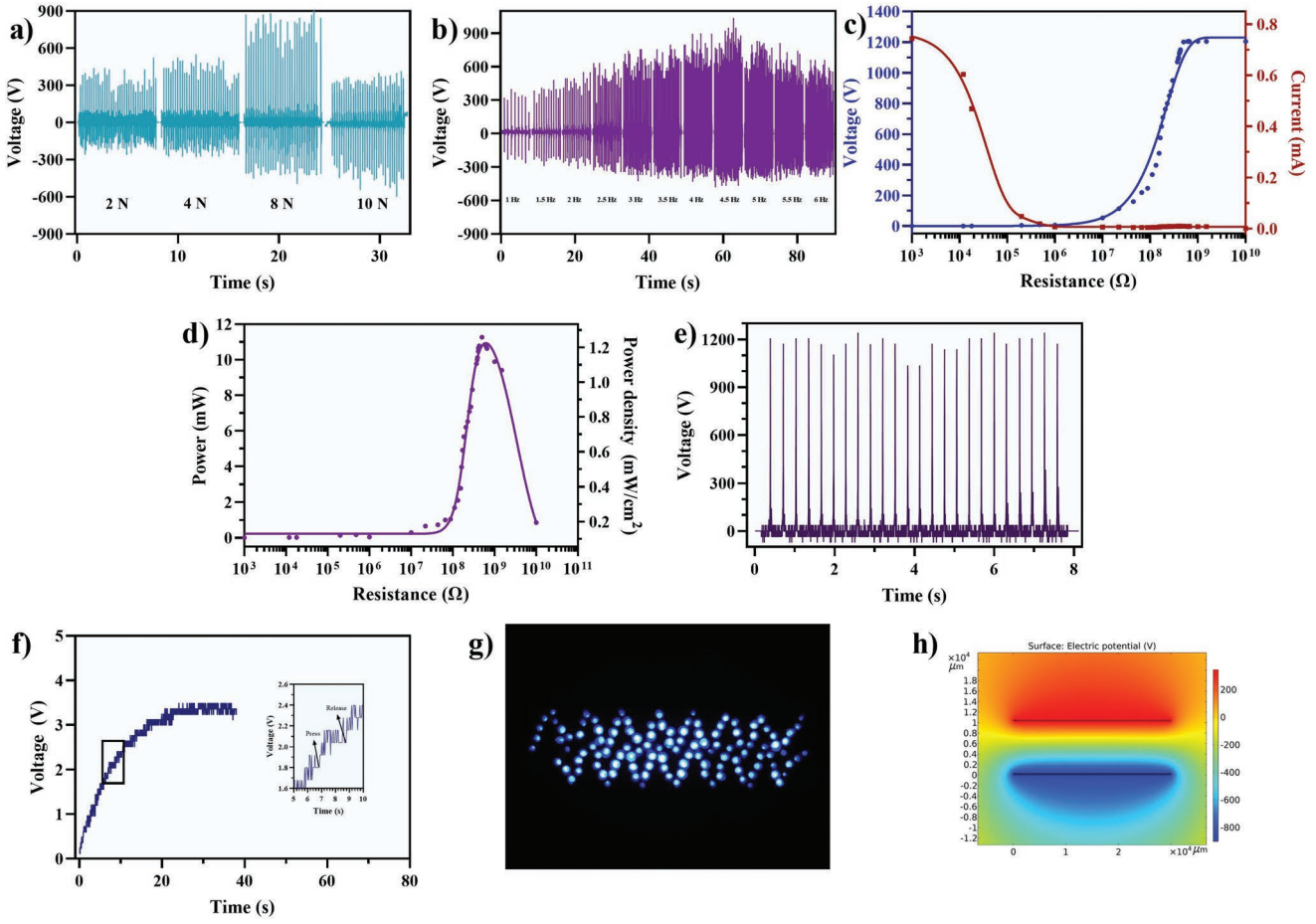

Figure 5. PPMA TENG outputs. a) Force and b) frequency optimization, c) output voltage and current against different external resistors, d) relationship between power, power density, and matching resistance, e) rectified open-circuit voltage of PPMA TENG, f) charging of a 1 µF capacitor, and g) illuminating 115 commercial LEDs with PPMA TENG. h) Electrical potential distribution results derived using COMSOL Multiphysics.

© 2023 The Authors. Advanced Electronic Materials published by Wiley-VCH GmbH

2199160x, 2023, 5, Downloaded from https://onlinelibrary.wiley.com/doi/10.1002/aelm.202201348 by Test, Wiley Online Library on [22/05/2023]. See the Terms and Conditions (https://onlinelibrary.wiley.com/terms-and-conditions) on Wiley Online Library for rules of use; OA articles are governed by the applicable Creative Commons License

ADVANCED ELECTRONIC MATERIALS
Open Access
www.advelectronicmat.de

is prevalent in TENGs; at elevated frequencies, the contact cycle is insufficient which means the succeeding cycle initiates before the previous cycle is completed. Therefore, PPMA TENG output at 6 Hz was ≈500 V. To further investigate the performance of PPMA TENG, its output was evaluated under various external loads ranging from 10^3 to 10^{10} Ω. Figure 5c represents the current and voltage under multiple loads. Short-circuit condition was established at low loads where the current reached its maximum value of 0.74 mA. Once the external resistance was increased, the voltage was raised, and the current gradually declined until the open-circuit condition was achieved at 632 MΩ and voltage saturated and reached a plateau at ≈1200 V. Figure 5d shows the power and the power density of PPMA TENG, which their maximum value was 11.27 mW and 1.25 mW cm^{-2}, respectively, at 500 MΩ. According to Figure S3, Supporting Information, a PPMA TENG without the MoS_2 monolayer, but with the same thickness, has open-circuit voltage, short-circuit current, and power of 143 V, 0.13 mA, and 0.12 mW respectively. This is an indication of the extensive effect of MoS_2 as an electron trap in PPMA TENG.

To determine the TENG function for practical applications, it was connected to a conventional full-bridge rectifier. The rectified voltage is displayed in Figure 5e. The rectified output was then used to charge a 1 µF capacitor to 3.3 V in 20 s with the rectified output. The charging of the capacitor is depicted in Figure 5f and the inset displays the charging curve with higher magnification. It could be concluded that a 0.24 µC charge was stored in the capacitor with each contact separation cycle. Additionally, the rectified TENG was connected to 115 commercial blue light-emitting diodes (LEDs) to assess its function under resistive load. PPMA TENG could successfully light up all the LEDs simultaneously (Figure 5g). To further investigate the principle of PPMA TENG, a finite element method using COMSOL Multiphysics was performed and the potential distribution of PPMA TENG was obtained (Figure 5h). The open-circuit voltage of PPMA TENG was calculated to be 1239 V by COMSOL which is only 3% different from the experimental result.

PPMA TENG is a contact-separation mode TENG which is a prominent nanogenerator. The working principle of this TENG is depicted in **Figure 6**a. Once AHSG as the positive layer is brought into contact with PS as the negative layer by an external force, a charge transfer from the positive to the negative layer occurs, which is due to the overlap of wave functions and different electronic structures. This is called contact

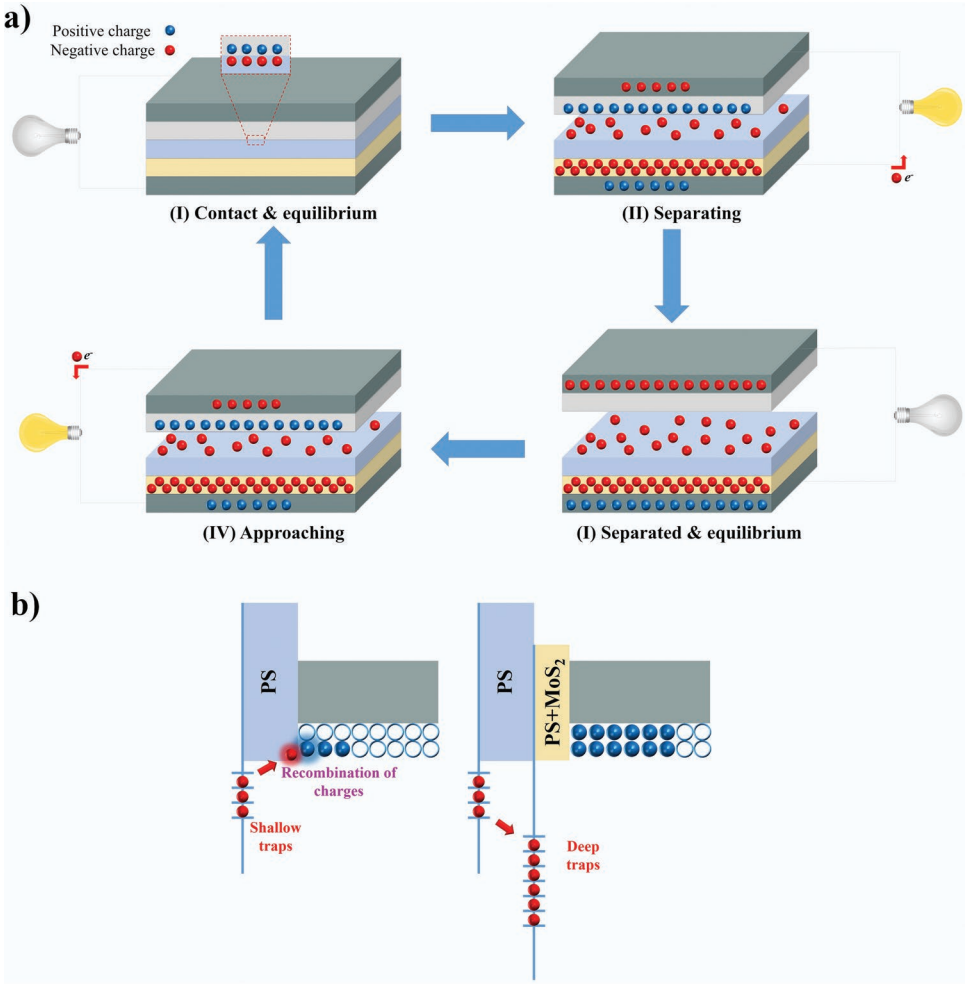

Figure 6. Working principles schematic. a) Working principles of PPMA TENG during contact-separation cycles. b) Charge trapping process in PS and PS+PS/MoS_2.

© 2023 The Authors. Advanced Electronic Materials published by Wiley-VCH GmbH

2199160x, 2023, 5, Downloaded from https://onlinelibrary.wiley.com/doi/10.1002/aelm.202201348 by Test, Wiley Online Library on [22/05/2023]. See the Terms and Conditions (https://onlinelibrary.wiley.com/terms-and-conditions) on Wiley Online Library for rules of use; OA articles are governed by the applicable Creative Commons License

electrification and until the layers are pressed together and the electrostatic equilibrium is maintained, no potential difference is observed (state I). By removing the force, layers separate and the charges on positive and negative layers are no longer in equilibrium (state II). Therefore, these electrostatic surface charges induce their counterpart on the back electrodes, which is called electrostatic induction. Connecting electrodes to an external circuit, a charge transfer from the bottom electrode to the top electrode could be observed to maintain another equilibrium and it is continued until the layers reach their maximum distance. While the layers reach their initial position, the electrodes saturate; hence there is no current between them (state III). Provided that TENG was subjected to a load again, as the layers move toward each other, electrons flow back from the top electrode to the bottom electrode (state IV).[39,40] By continuing this contact and separation process, an AC signal is produced, which could be employed for various applications.

In PPMA TENG, PS/MoS_2 layer under the negative contact layer acts as a negative charge storage layer. Figure 6b compares the charge trapping mechanism in a TENG with and without PS/MoS_2. After contact, both positive and negative triboelectric charges accumulated on the surface of contact materials. Without PS/MoS_2, if the contact materials separate, an electric field stemming from the induced positive charges on the bottom electrode attracts negative charges on the surface of PS. This electric field could be calculated using the following equation

$$E = -\frac{\sigma_T(x,t)}{\varepsilon_T \varepsilon_0} \quad (1)$$

where $\sigma_T(x,t)$ is the surface electrostatic charge, ε_T is the total permittivity of the combined PS+PS/MoS_2 layer, and ε_0 is vacuum permittivity. Furthermore, since these negative charges are stored in shallow traps, they drift toward the electrode under the influence of an electric field in dielectrics and combine with positive charges on the electrode. Inserting the PS/MoS_2 layer between the electrode and PS creates abundant deep trap sites, which could effectively trap negative charges and retard the drift process. Consequently, the induced charges in the bottom electrode rise, and this means the performance of the TENG improves.

To investigate the electron trap sites in PS/MoS_2, a Mott–Schottky plot of PS and PS/MoS_2 was obtained (**Figure 7**) using Equation (2)

$$\frac{1}{C^2} = \frac{2}{A^2 e \varepsilon \varepsilon_0 N_A}\left[(V - V_{FB}) - \frac{kT}{e}\right] \quad (2)$$

where C is space charge capacitance, A is the area of the film, e is electron charge (1.6×10^{-19} C), ε is the relative permittivity of film, ε_0 is vacuum permittivity (8.85×10^{-23} F m^{-1}), N_A is carrier density, V_{FB} is flat-band potential, k is Boltzmann constant (1.38×10^{-23} J K^{-1}), and T is temperature. The temperature term is generally small and can be neglected. The positive slope of the Mott–Schottky plot indicates the n-type behavior of PS/MoS_2 films. The x-axis intercept of the linear region in the Mott–Schottky plot determines the value of flat-band potential and the slop is $\frac{2}{A^2 e \varepsilon \varepsilon_0 N_A}$. Obviously, carrier density could be calculated from $N_A = \frac{2}{A^2 e \varepsilon \varepsilon_0 \times slope}$. The carrier density of PS/MoS_2 film was estimated at 1.9×10^{25} cm^{-3} using the above method. It is clear that the n-type behavior of PS/MoS_2 comes from the intrinsic n-type properties of MoS_2, which largely depends on interactions between MoS_2 and its surrounding.[41] Having the lowest formation energy, sulfur vacancies could be the origin of the n-type conductivity of MoS_2.[42] Rudimentary density function theory (DFT) calculations have demonstrated that sulfur vacancies introduce localized donor states in the bandgap, resulting in the generation of unpaired electrons into the lattice and thus n-type doping of the MoS_2.[43]

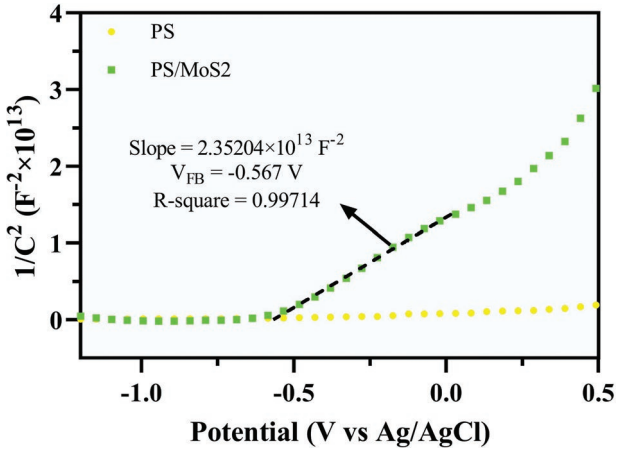

Figure 7. N-type behavior of PS/MoS_2. Mott–Schottky plot of PS and PS/MoS_2.

On the other hand, extensive DFT calculations indicated that the most abundant native defect (sulfur vacancy) in MoS_2 is either in a neutral or negative charge state. Therefore, being a deep acceptor, it cannot be the cause of the observed n-type properties.[44] In fact, the origin of the intrinsic semiconducting behavior of MoS_2 still remains unclear.[45] The inherent defects, such as sulfur vacancies, may not be efficient n-type dopants in MoS_2, although they could still act as a deep electron trap center,[46] suppressing the immigration of electrons toward electrodes in PS/MoS_2. It is worth mentioning that PS has also shown electron trapping ability due to the discontinuity of energy caused by benzene rings.[47,11] Therefore, the superior electron trapping behavior of the PS/MoS_2 composite could be due to the synergic effects of both MoS_2 and PS.

Durability is a vital property concerning the practical application of TENGs. PPMA TENG durability was assessed during 10 000 contact separation cycles. The open-circuit voltage was monitored at 5-min intervals during the first 1808 s and as it is shown in **Figure 8**a, no reduction was observed in the first 1808 s, but after 10 000 cycles, the average open circuit plummeted to 484 V. Nevertheless, after holding the PS+PS/MoS_2 layer in 70 °C for 3 h, an increase in the output of PPMA TENG was observed and the average open-circuit voltage reached 987.77 V. It was calculated that prior to the durability test, the surface charge of PPMA TENG was 1.067 μC m^{-2} whereas, after 10 000 cycles, it was declined to 0.428 μC m^{-2}. However, after annealing the PS+PS/MoS_2, the surface charge raised to 0.874 μC m^{-2} which was 82% of the initial value. This enhancement in the output

© 2023 The Authors. Advanced Electronic Materials published by Wiley-VCH GmbH

2199160x, 2023, 5, Downloaded from https://onlinelibrary.wiley.com/doi/10.1002/aelm.202201348 by Test, Wiley Online Library on [22/05/2023]. See the Terms and Conditions (https://onlinelibrary.wiley.com/terms-and-conditions) on Wiley Online Library for rules of use; OA articles are governed by the applicable Creative Commons License

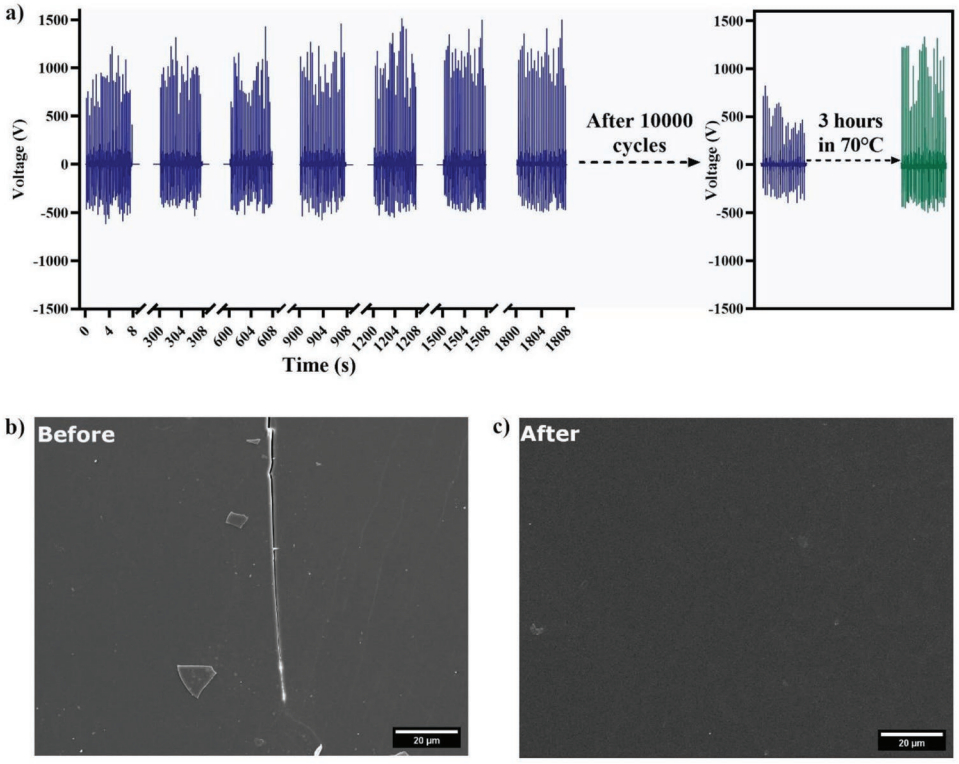

Figure 8. Durability test. a) Voltage of PPMA TENG during 1088 seconds (with 292 second intervals) and after 10 000 contact-separation cycles and after the self-healing process in the negative layer. The SEM image of PS surface b) before and c) after the self-healing process.

of PPMA TENG could be assigned to the self-healing of PS. It was reported by McGarel et al.[48] that surface cracks in PS films could be eliminated by heating. The primary mechanism for self-healing stimulated by heating is diffusion and randomization of minor polymer chains.[49–51] The PS surface before and after healing is shown in Figure 8c,d. Figure 8c depicts the surface of PS after 10 000 contact-separation cycles with a crack in the middle. After the healing process, there were no signs of cracks on the surface of PS meaning that the healing process was carried out successfully. After fully characterizing PPMA TENG, its application as a power source for a joining process will be discussed next.

Considering the AC nature of TENGs output, they could be employed to perform a nanoparticle joining process reported by Cha et al.[34] If the suspension of Ag NRs is subjected to a non-uniform electric field, the generated DEP force instigates the joining process of Ag NRs. **Figure 9**a depicts the FE-SEM images of Ag NRs prior to the joining process. The average width of synthesized Ag NRs was 112 ± 29 nm and their aspect ratio was estimated to be ≈9. Figure 9b demonstrates two NRs joined together by PPMA TENG. This assembly of NRs and their welding was also observed in other studies.[52] The schematic of the joining process setup is presented in Figure 9c. The assembled NRs not only attached but also welded together. Ag NRs on the Kapton were subjected to DEP, Lennard–Jones potential, and Coulomb forces. It was observed that DEP accumulates NRs near the tip of another NR to assist the joining process and for a cylindrical rod parallel to an electric field, it could be estimated using Equation (3)[53]

$$\vec{F}_{\mathrm{DEP}} = \frac{\pi r^2 L}{2}\varepsilon_{\mathrm{m}} Re\left[f_{\mathrm{CM}}\right]\vec{\nabla}\left|\vec{E}_{\mathrm{rms}}\right|^2 \tag{3}$$

where r is the radius, L is the length of NRs, $Re[f_{\mathrm{CM}}]$ is the real part of the Clausius–Mossotti factor, E_{rms} is the root-mean-square electric field, and ε_{m} is the real part of the complex permittivity of the surrounding medium of NRs. Obviously, electrophoresis force depends on the gradient of the electric field. To obtain a qualitative distribution of the electric field, COMSOL was employed and the result of modeling is depicted in Figure 9d when the voltage is 1200 V and the frequency is 4.5 Hz. This demonstrated that the electric field distribution in the space was equal and homogenous in a constant time.

The DEP force could successfully gather the NRs, but it is not sufficient to weld two NRs. In other words, NRs move in the direction of the electric field, and this transport due to DEP force increases the density of Ag NRs in the suitable position for joining. The joining occurs only when the concentration of Ag NRs accumulated at the tip of another Ag NR is sufficiently high to sustain the joining. Under the electric field, Ag NRs are charged with opposite polarity and the Coulomb force attracts the NRs and induces the welding while the Lennard–Jones force from the substrate account for the alignment of Ag NRs, consequently the tip of Ag NRs attach together leading to a tip-to-tip cold-welding.[34]

3. Conclusion

To conclude, PPMA TENG was fabricated using a straightforward spin-coating method in which a transparent bilayer

© 2023 The Authors. Advanced Electronic Materials published by Wiley-VCH GmbH

2199160x, 2023, 5, Downloaded from https://onlinelibrary.wiley.com/doi/10.1002/aelm.202201348 by Test, Wiley Online Library on [22/05/2023]. See the Terms and Conditions (https://onlinelibrary.wiley.com/terms-and-conditions) on Wiley Online Library for rules of use; OA articles are governed by the applicable Creative Commons License

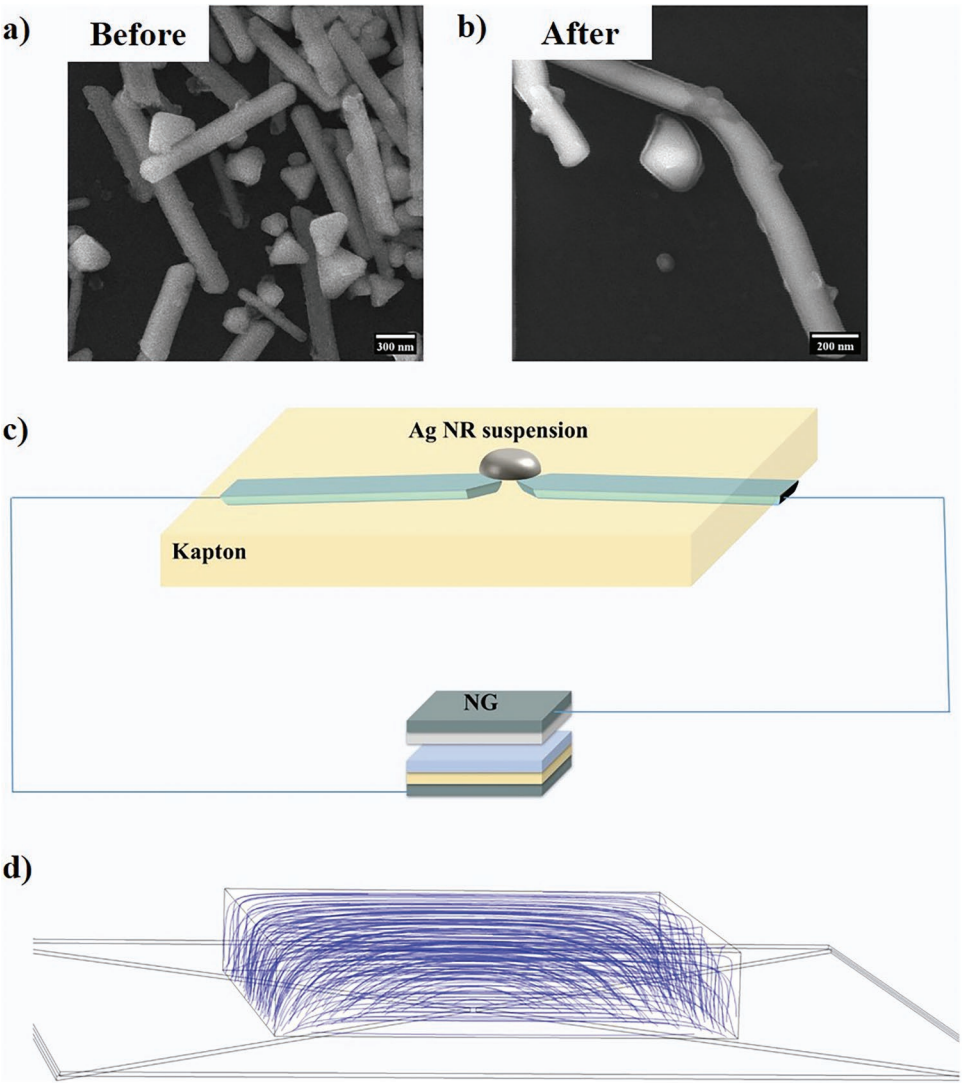

Figure 9. Welding of Ag NRs. FE-SEM images of Ag NRs a) before, b) after welding, and c) welding process schematic. d) Electric field simulation between two electrodes during the joining process.

of PS+PS/MoS_2 nanocomposite with 0.0300 ± 0.0003 mg exfoliated MoS_2 monolayers acted as negative friction and negative charge storage layer. The inherent defects, such as sulfur vacancies, in MoS_2 monolayers could act as a deep electron trap center, suppressing the immigration of electrons toward electrodes in PS/MoS_2 and significantly improving the output of the TENG. A novel AHSG layer was employed for the first time as the positive contact layer. The PPMA TENG showed an open-circuit voltage of ≈1200 V and a short-circuit current of 0.74 mA with a maximum power of 11.27 mW. For practical applications, 115 commercial blue LEDs were successfully illuminated, also a 1 µF capacitor was charged with the PPMA TENG which with each contact-separation cycle 0.24 µC was stored in the capacitor. This TENG manifested excellent durability before 10 000 cycles and after that, because of the self-healing properties of the negative layer, the output increases again given that the TENG was heated. It was proved that PPMA TENG could be successfully employed to weld Ag NRs together with the help of the AC nature of TENGs output.

4. Experimental Section

Materials: NMP, molybdenum(IV) sulfide (MoS_2) powder (<2 µm, 98%), polystyrene (pellets, average M_w = 350 000), polyvinylpyrrolidone (PVP) (M_w = 40 000), silver nitrate ($AgNO_3$), Iron(III) chloride hexahydrate ($FeCl_3.6H_2O$), and ethylene glycol were obtained from Sigma-Aldrich Co. and used without further purification. ITO/PET substrates (Nanogostar Sepahan Co., Iran) with a thickness of 175 µm and resistance of 15 ohm sq^{-1} were used as electrodes for TENG fabrication. Alyssum homolocarpum seeds were purchased from a local market. Cellulose tape (Top tape Co., China) was employed to adhere wires to the back of ITO electrodes. Ethylene-vinyl acetate (EVA) foam obtained from a local store was used as a protective layer around fabricated TENGs. Kapton sheet (Nanobazar Co., Iran) was utilized as an insulator for the cold-welding process.

© 2023 The Authors. Advanced Electronic Materials published by Wiley-VCH GmbH

2199160x, 2023, 5, Downloaded from https://onlinelibrary.wiley.com/doi/10.1002/aelm.202201348 by Test, Wiley Online Library on [22/05/2023]. See the Terms and Conditions (https://onlinelibrary.wiley.com/terms-and-conditions) on Wiley Online Library for rules of use; OA articles are governed by the applicable Creative Commons License

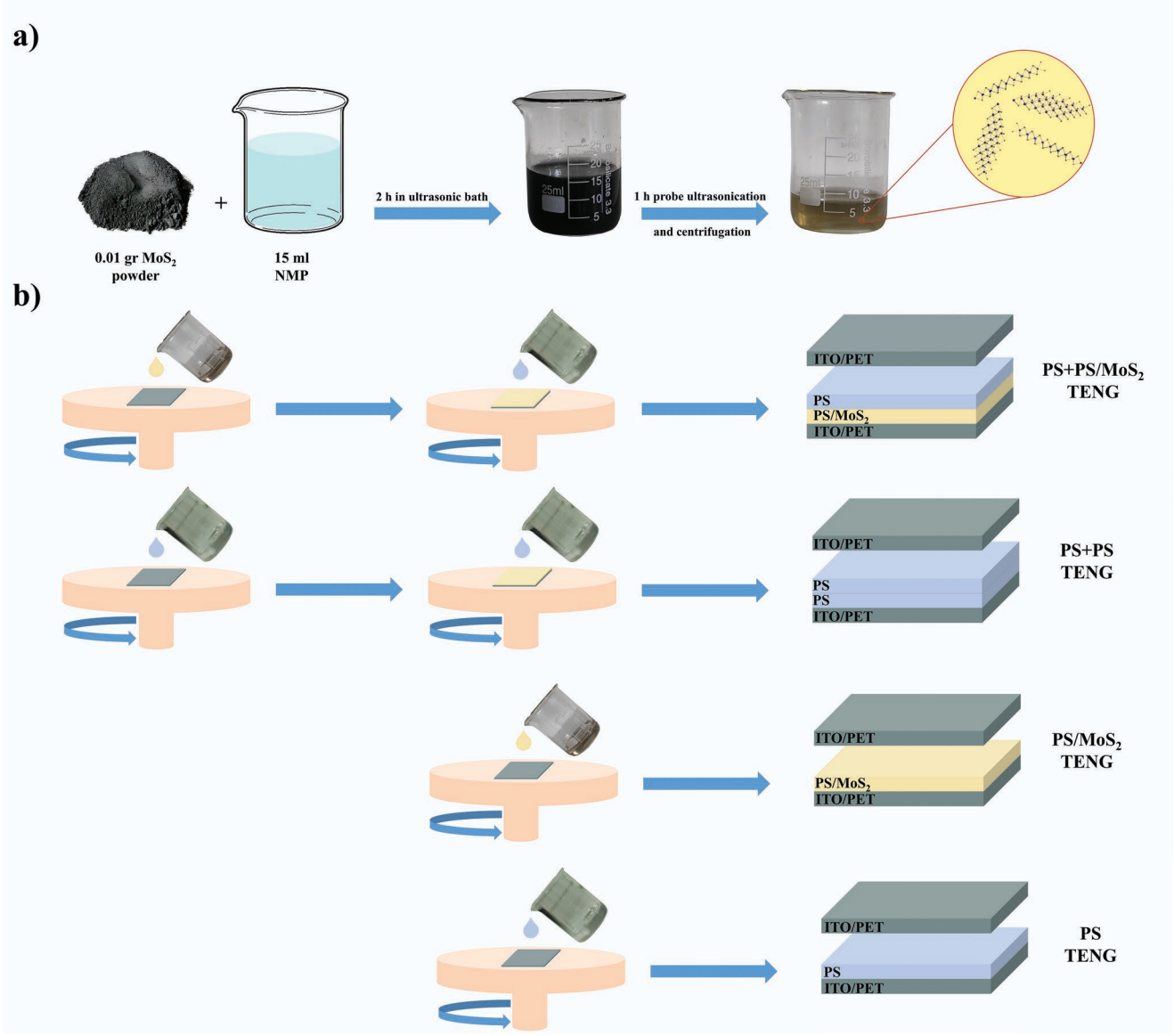

Figure 10. Fabrication process schematic. a) Exfoliation procedure of MoS_2. b) Manufacturing process of PS+PS/MoS_2, PS+PS, PS/MoS_2, and PS TENGs.

Preparation of MoS_2 Nanosheets: MoS_2 nanosheets were obtained by a modified liquid-phase exfoliation method.[54] After sonication, the prepared dispersion was centrifuged at 45 000 rpm for 45 min to remove the un-exfoliated MoS_2 flakes. The supernatant on top was carefully collected to avoid the un-exfoliated precipitates at the bottom of the falcon centrifuge tube. Finally, a dispersion with light yellow color was obtained and stored for further use. **Figure 10**a demonstrates a schematic of MoS_2 nanosheet preparation.

Fabrication of TENGs: 1.602 gr PS was solved in 3.642 gr NMP and then mixed with 0.878 gr MoS_2/NMP dispersion on a stirrer for 3 h at 60 °C. This solution was spin-coated on 3 × 3 cm^2 ITO/PET substrates with different speeds and a PS solution was also spin-coated on top of the PS/MoS_2 layer with several speeds to create the negative contact layer of TENG. All of the spin-coated films were dried at 60 °C for 3 h. This bi-layer structure formed the tribo-negative layer of TENG. Presumably, MoS_2 acted as a trap for electrons, and the PS/MoS_2 with a thickness of 25 µm was an electron storage layer. Copper wires were attached at the back of ITO/PET layers and the electrodes were adhered to a strip of EVA foam using cellulose tape. Finally, two ends of the EVA foam were attached using double-sided tape and two arc-shaped supports were created to maintain a 1 cm gap between positive and negative layers. This TENG was named PS+PS/MoS_2. In order to compare the electron storage ability of PS/MoS_2 nanocomposite with its contact electrification ability, a TENG named PS/MoS_2 consist of a single layer nanocomposite of PS/MoS_2 as negative contact layer and AHSG as positive contact layer with the same as-mentioned method was fabricated. Also, a TENG with a single PS layer as the negative layer and another TENG with a bilayer both made of PS was fabricated with the same method. Those two TENGs were labeled as PS and PS+PS, respectively. Figure 10b shows the fabrication process of these TENGs.

For fabrication of the tribo-positive layer, 0.166 gr AHSG was added to 5 mL deionized water and the dispersions were spin-coated on top of another ITO/PET substrate. The tribo-positive layer was dried at room temperature for 1 day. AHSG was extracted based on a method described by Koocheki et al.[55] Then a TENG consisting of PS+PS/MoS_2-AHSG called PPMA TENG was fabricated with the same method described above.

© 2023 The Authors. Advanced Electronic Materials published by Wiley-VCH GmbH

2199160x, 2023, 5, Downloaded from https://onlinelibrary.wiley.com/doi/10.1002/aelm.202201348 by Test, Wiley Online Library on [22/05/2023]. See the Terms and Conditions (https://onlinelibrary.wiley.com/terms-and-conditions) on Wiley Online Library for rules of use; OA articles are governed by the applicable Creative Commons License

Characterization of TENG Layers: SEM (Philips XL30 SERIES) was used to characterize the morphology of triboelectric layers. Before the imaging process, the samples were coated with a thin layer of gold. The synthesized MoS_2 monolayers were characterized by TEM (Zeiss-EM10C) operating at 100 kV. Also to determine the UV–vis spectra of MoS_2 monolayers, PS, PS/MoS_2, and PS layers, a UV–vis spectrophotometer (Metash-Model UV-6100 Series) was employed. The Mott–Schottky test was performed within the range from −1.5 to 0.5 V versus Ag/AgCl reference electrode a solution of 0.5 M Na_2SO_4 (pH = 7) was utilized as an inert electrolyte under a frequency of 1 kHz.

Characterization of TENG Device: The current was measured with a custom-built current preamplifier (CNI570).[56] The voltage was measured with digital oscilloscopes (MEGATEK-DSO5070 and Keithley 2450 sourcemeter). Also, the power and power density of TENG were evaluated using voltage and current. Furthermore, TENG was directly connected to LEDs to examine the operation of the TENG in practical conditions. In all measurements, the electrode attached to the PS+PS/MoS_2 was connected to the ground terminal of the oscilloscope, while the electrode attached to the AHSG layer was connected to the positive terminal. COMSOL Multiphysics software was used to perform finite element analysis. To calculate the potential distribution of PPMA TENG in the open-circuit condition, the electrostatic module was used. Moreover, the potential difference between electrodes was reported.

Supporting Information

Supporting Information is available from the Wiley Online Library or from the author.

Acknowledgements

This research did not receive any specific grant from funding agencies in the public, commercial, or not-for-profit sectors.

Conflict of Interest

The authors declare no conflict of interest.

Data Availability Statement

The data that support the findings of this study are available from the corresponding author upon reasonable request.

Keywords

2D materials, charge storage layers, energy harvesting, MoS_2, nanocomposite, nanoparticle welding, triboelectric nanogenerators

Received: January 2, 2023
Revised: February 2, 2023
Published online: March 22, 2023

[1] F. R. Fan, Z. Q. Tian, Z. L. Wang, *Nano Energy* **2012**, *1*, 328.
[2] Y. Zhou, W. Deng, J. Xu, J. Chen, *Cell Rep. Phys. Sci.* **2020**, *1*, 100142.
[3] Q. Shi, Z. Sun, Z. Zhang, C. Lee, *Research* **2021**, *2021*, 6849171.
[4] N. Cui, L. Gu, Y. Lei, J. Liu, Y. Qin, X. Ma, Y. Hao, Z. L. Wang, *ACS Nano* **2016**, *10*, 6131.
[5] Y. Liu, W. Liu, Z. Wang, W. He, Q. Tang, Y. Xi, X. Wang, H. Gou, C. Hu, *Nat. Commun.* **2020**, *11*, 1599.
[6] F. A. M. Rizk, G. N. Trinh, *High Voltage Engineering*, CRC Press, Boca Raton, FL **2014**.
[7] C. Zhang, L. Zhou, P. Cheng, X. Yin, D. Liu, X. Li, H. Guo, Z. L. Wang, J. Wang, *Appl. Mater. Today* **2020**, *18*, 100496.
[8] Y. S. Zhou, Y. Liu, G. Zhu, Z. H. Lin, C. Pan, Q. Jing, Z. L. Wang, *Nano Lett.* **2013**, *13*, 2771.
[9] X. Xie, X. Chen, C. Zhao, Y. Liu, X. Sun, C. Zhao, Z. Wen, *Nano Energy* **2021**, *79*, 105439.
[10] M. A. Jalili, Z. Khosroshahi, N. R. Kheirabadi, F. Karimzadeh, M. H. Enayati, *Nano Energy* **2021**, *90*, 106581.
[11] H. Wang, H. Sakamoto, H. Asai, J. H. Zhang, T. Meboso, Y. Uchiyama, E. Kobayashi, E. Takamura, S.-i. Suye, *Nano Energy* **2021**, *90*, 106515.
[12] N. R. Kheirabadi, N. S. Tabrizi, P. Sangpour, *J. Polym. Environ.* **2019**, *27*, 1642.
[13] C. Wu, T. W. Kim, H. Y. Choi, *Nano Energy* **2017**, *32*, 542.
[14] T. Huang, M. Lu, H. Yu, Q. Zhang, H. Wang, M. Zhu, *Sci. Rep.* **2015**, *5*, 13942.
[15] H. W. Park, N. D. Huynh, W. Kim, C. Lee, Y. Nam, S. Lee, K. B. Chung, D. Choi, *Nano Energy* **2018**, *50*, 9.
[16] C. Wu, T. W. Kim, J. H. Park, H. An, J. Shao, X. Chen, Z. L. Wang, *ACS Nano* **2017**, *11*, 8356.
[17] A. K. Singh, P. Kumar, D. J. Late, A. Kumar, S. Patel, J. Singh, *Appl. Mater. Today* **2018**, *13*, 242.
[18] *Two Dimensional Transition Metal Dichalcogenides* (Eds: N. S. Arul, V. D. Nithya), Springer, New York **2019**.
[19] A. V. Kolobov, J. Tominaga, *Two-Dimensional Transition-Metal Dichalcogenides*, Springer International Publishing, Springer, New York **2016**.
[20] J. N. Coleman, M. Lotya, A. O'Neill, S. D. Bergin, P. J. King, U. Khan, K. Young, A. Gaucher, S. De, R. J. Smith, I. V. Shvets, S. K. Arora, G. Stanton, H. Y. Kim, K. Lee, G. T. Kim, G. S. Duesberg, T. Hallam, J. J. Boland, J. J. Wang, J. F. Donegan, J. C. Grunlan, G. Moriarty, A. Shmeliov, R. J. Nicholls, J. M. Perkins, E. M. Grieveson, K. Theuwissen, D. W. McComb, P. D. Nellist, et al., *Science* **2011**, *331*, 568.
[21] L. Yuan, J. Ge, X. Peng, Q. Zhang, Z. Wu, Y. Jian, X. Xiong, H. Yin, J. Han, *AIP Adv.* **2016**, *6*, 125201.
[22] A. Kuc, N. Zibouche, T. Heine, *Phys. Rev. B: Condens. Matter Mater. Phys.* **2011**, *83*.
[23] O. Samy, S. Zeng, M. D. Birowosuto, A. El Moutaouakil, *Crystals* **2021**, *11*, 355.
[24] D. C. Espaciales, I. De Geofísica, **2015**, 799.
[25] A. Splendiani, L. Sun, Y. Zhang, T. Li, J. Kim, C. Y. Chim, G. Galli, F. Wang, *Nano Lett.* **2010**, *10*, 1271.
[26] Y. Jing, B. Liu, X. Zhu, F. Ouyang, J. Sun, Y. Zhou, *Nanophotonics* **2020**, *9*, 1675.
[27] S. A. Han, J. Lee, J. Lin, S. W. Kim, J. H. Kim, *Nano Energy* **2019**, *57*, 680.
[28] M. Seol, S. Kim, Y. Cho, K. E. Byun, H. Kim, J. Kim, S. K. Kim, S. W. Kim, H. J. Shin, S. Park, *Adv. Mater.* **2018**, *30*, 1870294.
[29] C. Gallardo-Vega, O. López-Lagunes, O. I. Nava-Galindo, A. De León, J. Romero-García, L. A. Aguilera-Cortés, J. Martínez-Castillo, A. L. Herrera-May, *Nanomaterials* **2021**, *11*, 1533.
[30] J. Yang, C. Yang, J. Cheng, A. Dai, T. Liu, Y. Yuan, K. Guo, D. Yuan, B. Wang, J. Lu, *Cell Rep. Phys. Sci.* **2020**, *1*, 100175.
[31] M. Kim, S. H. Kim, M. U. Park, C. J. Lee, M. Kim, Y. Yi, K. H. Yoo, *Nano Energy* **2019**, *65*, 104079.
[32] N. R. Kheirabadi, F. Karimzadeh, M. H. Enayati, E. N. Kalali, *Adv. Electron. Mater.* **2022**, *9*, 2200839.
[33] J. Luo, Z. L. Wang, *EcoMat* **2020**, *2*, e12059.

© 2023 The Authors. Advanced Electronic Materials published by Wiley-VCH GmbH

2199160x, 2023, 5, Downloaded from https://onlinelibrary.wiley.com/doi/10.1002/aelm.202201348 by Test, Wiley Online Library on [22/05/2023]. See the Terms and Conditions (https://onlinelibrary.wiley.com/terms-and-conditions) on Wiley Online Library for rules of use; OA articles are governed by the applicable Creative Commons License

[34] S. H. Cha, S. H. Kang, Y. J. Lee, J. H. Kim, E. Y. Ahn, Y. Park, S. Cho, *Sci. Rep.* **2019**, *9*, 3629.
[35] B. Sarno, D. Heineck, M. J. Heller, S. D. Ibsen, *Electrophoresis* **2021**, *42*, 539.
[36] S. M. Kim, J. Ha, J. B. Kim, *Integr. Ferroelectr.* **2016**, *176*, 283.
[37] J. Ha, S. M. Kim, J. B. Kim, *Integr. Ferroelectr.* **2017**, *183*, 171.
[38] B. G. Streetman, S. Banerjee, *Solid State Electronic Devices*, Pearson Education, Inc., **2014**.
[39] X. Feng, Q. Li, K. Wang, *ACS Appl. Mater. Interfaces* **2021**, *13*, 400.
[40] L. Zhou, D. Liu, J. Wang, Z. L. Wang, *Friction* **2020**, *8*, 481.
[41] K. Dolui, I. Rungger, S. Sanvito, *Phys. Rev. B: Condens. Matter Mater. Phys.* **2013**, *87*, 165402.
[42] W. Zhou, X. Zou, S. Najmaei, Z. Liu, Y. Shi, J. Kong, J. Lou, P. M. Ajayan, B. I. Yakobson, J. C. Idrobo, *Nano Lett.* **2013**, *13*, 2615.
[43] H. Qiu, T. Xu, Z. Wang, W. Ren, H. Nan, Z. Ni, Q. Chen, S. Yuan, F. Miao, F. Song, G. Long, Y. Shi, L. Sun, J. Wang, X. Wang, *Nat. Commun.* **2013**, *4*, 2642.
[44] J. Y. Noh, H. Kim, Y. S. Kim, *Phys. Rev. B: Condens. Matter Mater. Phys.* **2014**, *89*.
[45] A. Singh, A. K. Singh, *Phys. Rev. B* **2019**, *99*, 1.
[46] Ł. Gelczuk, J. Kopaczek, P. Scharoch, K. Komorowska, M. Blei, S. Tongay, R. Kudrawiec, *Phys Status Solidi RRL* **2020**, *14*, 2000381.
[47] Y. Yu, L. Y. Bian, J. G. Chen, Q. H. Ma, Y. X. Li, H. F. Ling, Q. Y. Feng, L. H. Xie, M. D. Yi, W. Huang, *Adv. Sci.* **2018**, *5*, 1800747.
[48] O. J. McGarel, R. P. Wool, *J. Polym. Sci., Part B: Polym. Phys.* **1987**, *25*, 2541.
[49] R. P. Wool, K. M. O'Connor, *J. Appl. Phys.* **1981**, *52*, 5953.
[50] Y. H. Kim, R. P. Wool, *Macromolecules* **1983**, *16*, 1115.
[51] T. C. Mauldin, M. R. Kessler, *Int. Mater. Rev.* **2010**, *55*, 317.
[52] G. González-Rubio, J. González-Izquierdo, L. Bañares, G. Tardajos, A. Rivera, T. Altantzis, S. Bals, O. Peña-Rodríguez, A. Guerrero-Martínez, L. M. Liz-Marzán, *Nano Lett.* **2015**, *15*, 8282.
[53] A. I. Baca, J. J. Brown, K. A. Bertness, V. M. Bright, *Nanotechnology* **2012**, *23*, 245301.
[54] Y. Wei, *Preparation and Characterization of Liquid Phase Exfoliated MoS2 Nanosheets*, University of Alberta, Alberta, Canada **2018**.
[55] A. Koocheki, S. A. Mortazavi, F. Shahidi, S. M. A. Razavi, R. Kadkhodaee, J. M. Milani, *J. Food Process Eng.* **2010**, *33*, 861.
[56] S. S. K. Mallineni, H. Behlow, R. Podila, A. M. Rao, *Nanotechnol. Rev.* **2018**, *7*, 149.

© 2023 The Authors. Advanced Electronic Materials published by Wiley-VCH GmbH

2199160x, 2023, 5, Downloaded from https://onlinelibrary.wiley.com/doi/10.1002/aelm.202201348 by Test, Wiley Online Library on [22/05/2023]. See the Terms and Conditions (https://onlinelibrary.wiley.com/terms-and-conditions) on Wiley Online Library for rules of use; OA articles are governed by the applicable Creative Commons License